RESEARCH ARTICLE

In-Situ Process Monitoring and Defects Detection Based on Geometrical Topography With Streaming Point Cloud Processing in Directed Energy Deposition

MUHAMMAD MU'AZ IMRAN[1,2]**, YOUNG KIM**[1]**, GISUN JUNG**[1]**,
LIYANAGE CHANDRATILAK DE SILVA**[2]**, (Senior Member, IEEE),
JEONG-HUN SUH**[3]**, PG EMEROYLARIFFION ABAS**[2]**, AND YUN BAE KIM**[1]

[1]Department of Industrial Engineering, Sungkyunkwan University, Suwon 16419, South Korea
[2]Faculty of Integrated Technologies, Universiti Brunei Darussalam, Gadong BE1410, Brunei Darussalam
[3]Digital Manufacturing (DM) Laboratory, Hwacheon Machinery Company Ltd., Gwangju 506-733, South Korea

Corresponding authors: Pg Emeroylariffion Abas (emeroylariffion.abas@ubd.edu.bn) and Yun Bae Kim (kimyb@skku.edu)

ABSTRACT The 3D printing industry faces challenges in ensuring reliable and repeatable processes, as increasing slopes can lead to defects and faults forming layer by layer in fabricated parts. Detecting these defects through post-processing quality inspections is time-consuming and laborious. To address this, a new method is proposed that incorporates a scoring scheme to quantitatively evaluate process performance using clad height data during printing. This approach aims to save time and cost while preserving the structural integrity of the part. The study develops a layer-wise point cloud processing technique to convert the incoming unordered data streams into rasterized points. By transforming raw signals into spatially equidistant points representing clad height in a 2-D Cartesian plane, a heatmap tomography of each layer is generated. Subsequently, a novel *Defects-Finder* algorithm is developed to locate and cluster surface defects based on the assigned scores. The findings demonstrate the algorithm's ability to identify the root cause of propagated faults, which can result in severe defects. Additionally, the study employs various statistical measures in the layer-level analysis to evaluate miniature process faults or shifts, which may get overshadowed, including cases of under and over-deposition. Through comparison and validation with physical artifacts, the proposed method proves effective in identifying and assessing process faults. Ultimately, this method enhances big data visualization for cost-effective quality control and boosts the overall productivity of additive manufacturing processes. By streamlining defect detection and performance evaluation, it addresses the challenges faced by the industry in ensuring reliable 3D printing outcomes.

INDEX TERMS Big data visualization, directed energy deposition, in-situ quality monitoring, performance evaluation, surface defects detection.

I. INTRODUCTION

The recent decades have seen a paradigm shift in structural and product design due to the advancement of Additive

Manufacturing (AM) and, more importantly, how things are sustainably fabricated; A layer-wise approach as opposed to the conventional Subtractive Manufacturing (SM) method. The core principle of SM is the removal of materials via machining, drilling, grinding, or casting into moulds. Research has consistently shown that SM suffers from a

The associate editor coordinating the review of this manuscript and approving it for publication was Manuel Rosa-Zurera.

lower-level design freedom [1]. In contrast, AM, commonly referred to as '3D printing', empowers end-users to produce crucial spare parts that are intricate and costly [2]. Hence, it has taken a central stage in the transformation of supply chains in the new global economy. Other benefits of leveraging on AM include reductions in the (1) associated costs from the direct reduction of manufacturing lifecycle costs and non-recurring costs, (2) lead time, and (3) mass of the components [3]. Indeed, this disruptive technology has become part and parcel of today's competitive market and has expanded into several sectors, including the military, aerospace, medical, automotive, and dental industries [4].

The two common metal-AM technologies are selective laser melting (SLM) and directed energy deposition (DED). SLM technology employs layer-by-layer fabrication, and hence, it has limited scalability (build volume). For SLM to scale, a larger build container is required to satisfy the maximum dimensions of the build and must be filled with feedstock materials. On the other hand, DED allows freeform fabrication, with DED scalability limited by the scalability of the robotic and gantry systems. Also, DED stores feedstock in a separate refillable container, pumps it to the deposition head and melts it locally. As such, DED has gained popularity over SLM.

The fundamental process involved in DED is the use of a highly focused energy beam to instantaneously liquefy feedstock and substrate materials, forming a molten pool that steadily solidifies as the beam maneuvers, guided by the pre-set trajectories. Unlike SLM, DED can be exclusively used for repair or retrofitting by leveraging its multiple-axis features and its ability to produce functionally graded materials (FGM) [5]. However, the capability of DED to manufacture complex structures is often limited, and it frequently suffers from lower geometrical accuracy and surface quality [6]. The generalization of DED technology also poses a challenge; optimized process parameters for a specific part's structure may not produce the same outcomes when used for printing another part design, regardless of identical material used [7]. Despite these challenges, advancements in DED technology have allowed DED to produce results comparable to those of SLM.

Another challenge in the DED process is that it involves many processing parameters that are confined to a brief processing window. Process faults, including pores, edge collapsing, and under and over-deposition, are often inevitable [8] but can be minimized. To date, a series of post-processing methods is required to inspect and evaluate the quality of manufactured parts and determine their conformance to the required standards. Chen et al. [9] asserted that extra effort is required to develop AM standards, that is, quality assurance. Furthermore, the evaluation process, either via non-destructive methods (e.g., X-ray, ultrasonic, callipers, machine vision, and roughness testing) or destructive methods (e.g., cutting into smaller samples) [10], can be costly and time-consuming. Once evaluated, the parts may need to be

sent for further post-processing to improve their surface finish and mechanical properties [11]. Naturally, this long-chain process reduces AM productivity.

Alternatively, the value of in-situ monitoring a manufacturing process is now widely acknowledged by the AM industry [12]. Manufacturers of AM machines have started incorporating a diverse range of sensors into their latest models for monitoring purposes, whilst at the same time, to understand the relationship between process variables and part properties [13], [14], [15], [16]. In-line inspection has become increasingly necessary [17], [18]. This is because sensor data, combined with the AM machine axes, can be recorded to show a complete timeline and location history of the variable during the deposition process [19].

However, big data mining in AM, particularly with DED, has made limited progress so far [20], [21]. Data mining involves analyzing data collections with statistics, mathematics, computer algorithms, and graphics to uncover meaningful information and patterns [22]. Visualization techniques can make data mining even more effective in additive manufacturing [23], and its aims usually vary naturally across industries, with various available data taxonomies [24]. Posada et al. [25] speculated that big data visualization is already becoming indispensable and will remain relevant in Industry 4.0, as it caters to more comprehensive and integrated solutions. A wide range of algorithms already exists for big data visualization, whether for quality monitoring or defect detection [26]. However, there is a need for statistical methods that can automatically detect onset defects [27], particularly in detecting small process shifts [28].

To support the ongoing advancement of in situ monitoring, it is crucial to create adaptable techniques that can register and combine various data types, including sensor readings, machine scan paths, and log files, and churn out meaningful information from the data [29]. This paper is exactly intended to fill in this research gap, by developing a framework that can assess the performance of the deposition process in real-time. The contributions from this research are:

- Devising a real-time rasterization method that can transforms incoming data streams into an ordered point cloud data structure in real-time. This is achieved by using raster cells/voxels to represent the clad height of adjacent raw data points. The proposed method was validated with batch (near real-time) processing as a benchmark using the Mean Squared Error (MSE). The deviation between the observed melt-pool height data and the nominal threshold value is calculated for each cell/voxel, and the percentage deviation is apportioned into intervals.
- Layerwise heatmap topography based on assigned scores can be used to provide visualization, aiming to provide information pertaining to the state of the layer and statistical accessors to detect process shifts on each layer. These preprocessing steps are essential for downstream analysis.

- Finally, a novel defects-finder algorithm is proposed as a by-product of our framework that iteratively searches for clusters of defects upon the completion of each layer. To validate our algorithm, a basis on a-priori-identification is applied, which involves validating by cross-comparison to data gained from ex-situ measurements, i.e., visual inspections, of defects at the exact locations [30].

The paper is organised into multiple sections. Section II: Related Works outlines relevant works, including types of defects, geometrical sensing, and point cloud processing. Next, Section III: Materials and Methods outlines the equipment utilised for data collection and the proposed framework, which encompasses details on batch and streaming phases, preprocessing steps, performance evaluation, and the defects-finder algorithm. In Section IV: Results and Discussion, we delve into the experimental setups, validate the streaming algorithm's effectiveness through batch processing, analyse the proposed method at the layer level, and examine the results of the surface defects cluster. Finally, concluding remarks are offered in the conclusion section.

II. RELATED WORKS

A. TYPES OF DEFECTS

Significant analysis and discussions on the geometrical defects related to DED was presented by AbouelNour and Gupta [30] and Zehao et al. [28] The intricacies of the printing process may result in flaws which may manifest at any stage of the printing process and these flaws can significantly impact the quality and strength of the printed parts. Flaws may not be immediately visible and rectify these flaws post-production may be challenging due to the large build size and complex geometries, that could not be easily seen, let alone, reached for post-processing rectification. Defects can generally be categorized into three classes: (1) surface defect, which is easily visible on the outer surface; (2) subsurface defect, which occurs within a depth of 1-500 μm below the surface; and (3) internal defect, which is located at depths greater than 500 μm, and can manifest in the shape of pores, voids, or cracks [30], [31]. These defects can be infinitesimal in size at their incipient stage. It is important to meticulously monitor each layer of the printing process, to detect any deviations from the norm as early as possible. By doing so, the machine operator can make informed decisions that may help minimize defects and maintain a high level of control over the entire process to ensure consistency and reproducibility of the process [32].

B. GEOMETRICAL SENSING

Several researchers have proposed in-situ monitoring using different sensors. This facilitates the collection and understanding of process signatures, including the molten pool temperature distribution and its gradient or geometrical characteristics (i.e., the height, width, dilution, or wetting angle and shape), and ultimately, can be used to identify

flaws during the manufacturing process. Indeed, previous studies have reported that a correlation exists between different process signatures and the quality of fabricated parts [16]. Thus, monitoring of process signature allows the computer or operator to adjust the parameters during the manufacturing process or stop lengthy processes if any defects or deviations occur to avoid wasting manufacturing time and resources. However, these process signatures are difficult to interpret and require several preprocessing and feature extraction techniques to convert them into meaningful information for speeding up diagnostics in the context of quality [33], [34]. Typically, a machine operator is responsible for monitoring and intervening when faults occur. Typically, once suitable process parameters and signatures for the monitoring process are identified, suitable means of monitoring the parameters and signatures need to be selected. For instance, monitoring of geometrical and thermal characteristics can be achieved through the utilization of image signals with a visible (CCD/CMOS camera or 3D scanner/projector) and an infrared spectrum, respectively. Xia et al. [35] provided a comprehensive overview of various methods for monitoring and detecting different kinds of defects, helping to guide the selection process.

In this study, the focus is to monitor the geometrical accuracy of the build parts; to detect normal, under- and over-deposition. There are two monitoring approaches of obtaining geometrical process signatures [16], [36]: laser scanning-based [37], [38], [39], [40], [41], [42] and machine vision-based [43], [44], [45], [46], [47], [48], each with their strengths and weaknesses. Laser scanning-based monitoring system has been used to obtain more precise depth information on fabricated parts, i.e. layer height, by obtaining high-density data in 3D coordinate systems known as point clouds [41]. Point clouds are highly sensitive to geometric variations, surpassing images in their ability to detect even the smallest defects in the manufacturing process. However, laser scanning-based monitoring system has severe limitations, especially when it comes to in-situ monitoring of metal AM processes. Firstly, the ineffectiveness of laser scanning for in-situ monitoring of a molten pool stems from the obstructions of the camera's structured light caused by the intense light radiated by the pool [16], [38]. Secondly, scanning with a detector may encounter two potential issues that can cause misleading inferences. The first is the occlusion effect [49], where the scanner scans the surface, but the detector cannot see the region, and the second is the shadow effect [41], [49], [50], which occurs when the part design has complex shapes or due to surface irregularities that prevent some regions from being reached by the laser scanner. Thirdly, as laser scanning-based systems have limited surface area coverage [38], the entire surface area must be scanned iteratively line-by-line, causing longer lead times. This is especially true in some industries, such as the aerospace industry, where larger components are common [3]. To guarantee adequate coverage, a sizable laser scanning-based system may be required,

but this comes at the expense of rising the overall manufacturing costs. Finally, most laser scanning-based technology currently available is used for inspection after construction. While it is possible to monitor upon the completion of each layer, this would limit its processing capability to near-real-time only [36], [38], [41], [50]. This delay would lengthen the lead time by factoring in the time needed to scan the entire surface area of the build.

On the other hand, machine vision is cost-effective and compatible with various systems, particularly for in-situ monitoring, providing detailed contextual information for downstream analysis. Most of the metal AM equipment already uses at least a binocular vision system [43], [46], [51]; thus, depth measurement can already be attained [52]. However, the system's reliability depends heavily on the lighting conditions, which greatly influences the benchmarks. Additionally, machine vision-based 2D monitoring systems struggle to accurately capture depth information with a single camera setup, and as such, adding more cameras to the setup may be able to improve accuracy and reliability [16]. There is strong evidence, as suggested by Chua et al. [53], to support the use of complementary metal-oxide semiconductor (CMOS) cameras for single-layer inspection, which involves monitoring the process signature of the melt pool geometry and using the information to control laser power. Multi-layer inspections, both in-situ and ex-situ, have also been recommended in order to identify flaws in the multiple layers and determine their size. Traditionally, non-destructive tests using X-ray and CT scans have been used for this purpose. This type of inspection can reveal surface, sub-surface, and internal defects, including voids and porosities, as well as their relative positions. However, for this particular study, the focus is solely on identifying surface defects on the basis of geometrical process signatures.

C. POINT CLOUD PROCESSING

Rasterization is commonly employed to process high-dimensional unordered point clouds, transforming them into ordered point clouds or images to enhance the performance of downstream algorithms [54]. Lyu and Manoochechri [41] developed an online laser scanning system that efficiently monitors the Fused Filament Fabrication (FFF) process. The system uses a custom program that reduces noise with a point cloud library (PCL) [55] and extracts the upper surface of the part with the RANSAC algorithm [56]. Subsequently, a rasterization method was used to explain surface quality by calculating the depth of each grid node based on the distance of accumulated neighbouring projected scanned points—the ratio of grid depth to the designed layer thickness was used to identify over and under extrusions through colour coding. Afterwards, a CNN model was used to classify the state of a manually labelled layer into four main classes: normal, under-deposition, over-deposition, and severe under-deposition, and based on the classification results, the process parameters

were adjusted for the subsequent layer. However, generally labelling the whole layer as having either of the three anomaly classes based on only some areas of the layer with defects could result in issues for the previously deposited normal areas. This is because, whilst the adjusted process parameters may be suitable for some of the layers with defect, it may not be suitable for the layer as a whole. Localizing these defects separately with multi-classification and make the appropriate adjustments to the process parameters solely in those affected regions would have been a more productive actions.

Similarly, Ye et al. [57] used the rasterization technique for point cloud transformation, however, they have asserted that the technique is insufficient for detecting defects and that only minor differences can be observed when comparing the distributions of the rasterized pixels. Ye et al. [28] proposed a framework for detecting manufacturing process defects using in-situ point clouds. A series of preprocessing steps, including translation, orientation, and scaling, was used to measure the planes' affinity between the unordered and reference point clouds to describe the surface variations. This was necessary since the captured point clouds were not on the same plane.

Point cloud data structure can be further leveraged for a follow-up analysis to identify surface, sub-surface and internal defects. Kalami and Urbanic [49] used point cloud data to establish a correlation with surface roughness. This non-destructive approach formed an integral part of a post-processing procedure, whereby surface roughness results were subsequently compared with those obtained from destructive testing. Petrich et al. [58] combined toolpath data with process signatures to form a point cloud after each layer was fabricated. Subsequently, the point cloud was converted into a raster image, with pixel values assigned based on the average of the nearest data points. Additionally, a homography technique was used to align the registered computerised tomography (CT) and layerwise electro-optical imagery data with the toolpath through iterative optimization. With this technique, spatial and temporal data were integrated through synchronization. Subsequently, clusters of anomalous CT voxels could be detected based on the CT scan's grayscale intensity.

The use of point clouds in metal AM for in-situ inspection, however, remains limited, as most studies have focused on post-processing approach. Gronle et al. [59] visualized the unordered point cloud representation of each layer's raw InGaAs photodiode signal. Chen et al. [60] exploited unordered point clouds obtained from a laser profiler to detect surface defects through unsupervised and supervised machine learning methods. Initially, DBSCAN clustering was used to segregate the point cloud regions that may contain surface defects. Subsequently, the clustering outcomes were fed into a supervised classification algorithm to classify the type of defects. Garmendia et al. [61] used third-party GOM inspection software to visualize the layer height deviations. However, the software's capability is limited to visualizing the deviations of the outer surface of the manufactured part
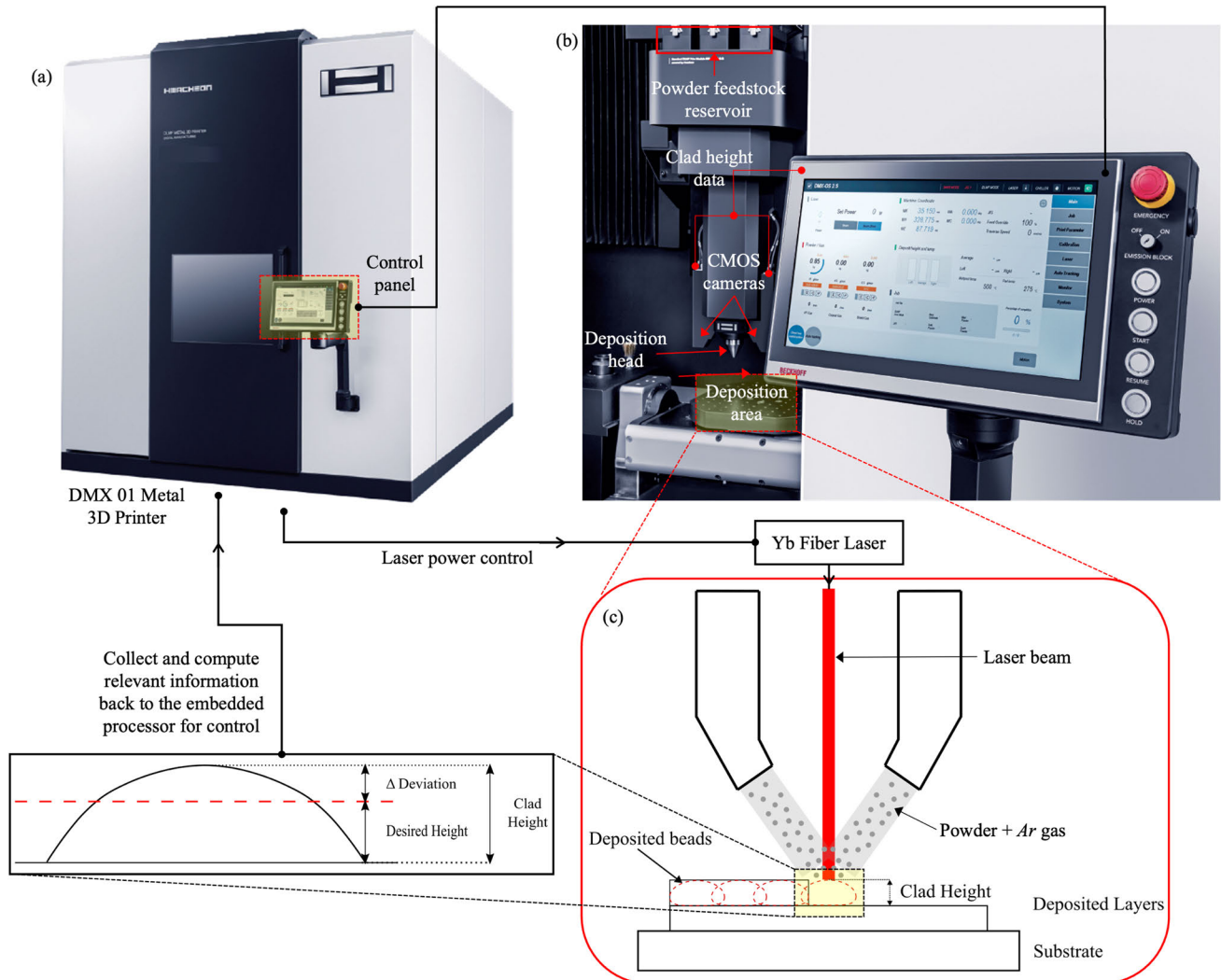
FIGURE 1. A schematic diagram of DLMF system hardware: (a) DMX 01 Metal 3D printer, (b) DMX 01 deposition head (Standard DLMF Print Module 800) that is equipped with dual machine vision-based (CMOS) cameras and powder feeder delivery system, along with a magnified control panel, and (c) DLMF process illustrating the laser-powder interaction with its resultant clad.

only and not the internal segment. In real industrial settings, it is essential to ensure the reliability of parts; therefore, information on the internal section of the part is also necessary to prevent the need for destructive testing. Meanwhile, Bernhard et al. [62] tackled this problem by transforming the unordered toolpath coordinates into ordered point clouds, each pixel representing the melt-pool temperature data using OCTAVE software to enable the in-line inspection. However, quantifiable results of the process performance were not presented. Furthermore, visualization was only created once the print was completed and not in a layer-wise manner—relying on third-party software. In contrast, Heralić et al. [38] introduced a simple preprocessing technique to transform the sampling points into a set of N discrete points along the deposition toolpath. Instead of temperature data, they measured the performance of the process by measuring the error between the mean of the layer height and the reference height of the robot.

However, this approach does not capture information between the layers; that is, if the layer has small, accumulated layer-by-layer defects; hence, localizing these faults or errors on the layer is not possible.

III. MATERIALS AND METHODS
A. HARDWARE SETUPS AND DATA ACQUISITION
In-situ process monitoring data was acquired on a direct laser metal forming (DLMF) process, which is a type of DED process, on a DMX 01 Metal 3D printer, as shown in Fig. 1. A close inspection of the DMX 01 deposition head in Fig. 1 reveals an integrated system comprising an intricate powder delivery system, with a dual vision-based monitoring system. The DMX 01 utilizes a coaxial nozzle design that allows the powder stream assisted by the carrier gas to enclose the Ytterbium (Yb) fiber laser beam into a conical shape protected
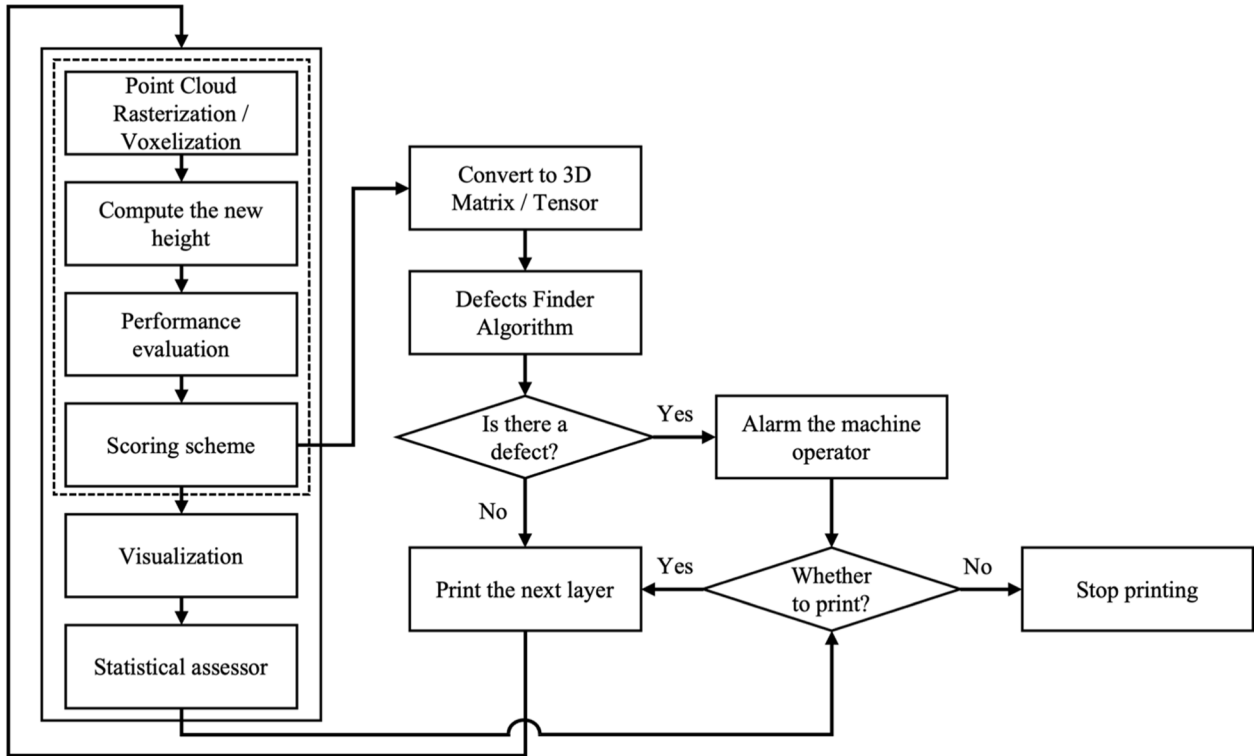
FIGURE 2. The proposed framework architecture for process in-situ monitoring and defects detection based on point cloud processing.

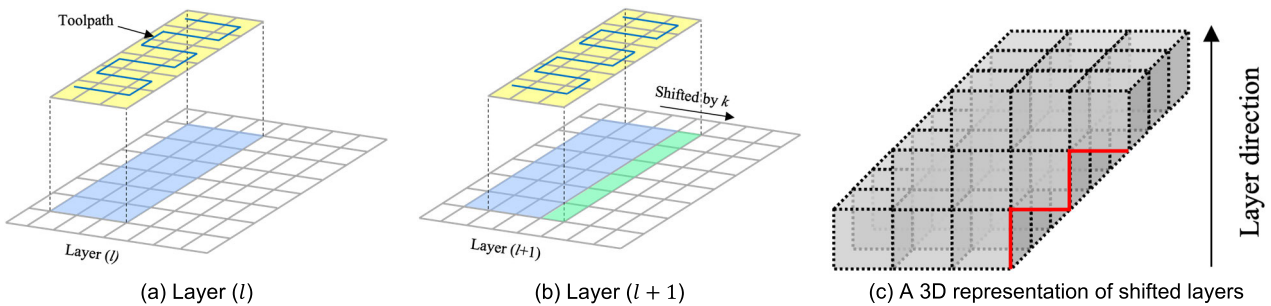| (a) Layer (l) | (b) Layer ($l + 1$) | (c) A 3D representation of shifted layers |

FIGURE 3. An ordered point cloud data structure: (a) indicates the prior layer deposition, (b) shows the next layer deposition shifted by the k step due to the inclined slope. (Yellow, Blue, and Green colours represent the local, global, and new subdivisions, respectively), (c) An ordered point cloud structure of the shifted layers in a 3D representation while structuring the pixels (X- and Y-coordinates) within the corresponding Z-direction; leaving the unsupported layers (overhangs), which are marked by a red line.

by the shielding gas (Argon gas) to avoid oxidation. The distance between the workpiece and nozzle has been adjusted to a 9mm offset. A machine vision-based monitoring system, developed based on the US7423236B2 patent [63], using dual complementary metal-oxide-semiconductor (CMOS) cameras are used. The cameras are mounted off-axially to obtain the melt pool height data [16], [64], [65]. The pixel is about 800×600 with a frame rate of 60 Hz. Toolpath trajectories or scan vectors are logged by the machine and contain information regarding the AM build strategy, including (i) time, (ii) laser position, (iii) laser power, and (iv) melt pool height. Variations in the melt pool can be adjusted by utilizing laser power as the controller parameter due to its instantaneous

response rate from the external control signal. Comparatively, mechanical-based motion control is slower, i.e., scanning speed. Powder flow control is even slower, causing a delay in the order of seconds from powder reservoirs [46].

B. OVERVIEW OF THE PROPOSED FRAMEWORK
Flowchart representation of the proposed framework is given in Fig. 2. The real-time rasterization technique transforms the unordered point cloud of the incoming data streams, including process signature information, into spatially coordinated equidistant coordinates. In this work, the point cloud generation involves a 5D data stream (x, y, z, t, h), where x, y and z are coordinates, t is the time index and h is the clad
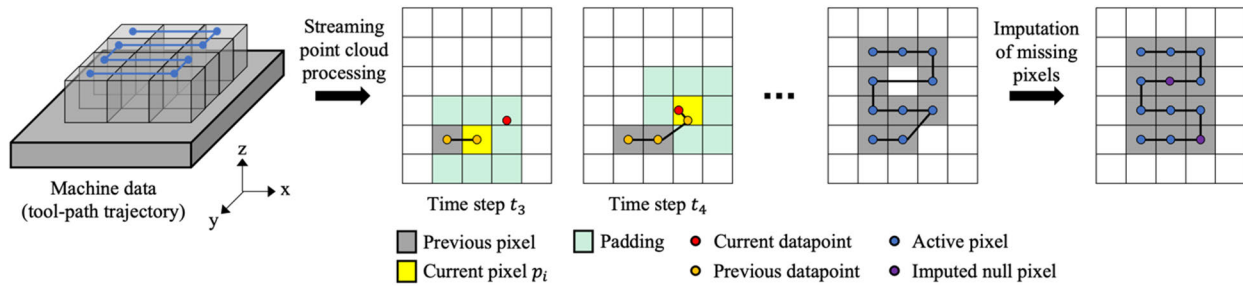
FIGURE 4. A schematic of real-time rasterization of the point cloud process flow.

height. Clad height is included as part of the layer-wise monitoring and addresses the critical challenges of information processing posed by the existing point cloud generation using existing point cloud-based approaches. Point clouds captured by laser scanning-based or process information logged by the machine often have an unordered data structure, as AM products are frequently associated with freeform geometries (arbitrary toolpath) with different shape at every layer. Therefore, the proposed method addresses these issues by considering the points ordering based on the prior layers, as shown in Fig. 3. As clad height at the current layer is affected by the clad height at the previous layer, re-computation of the new height representing each raster/voxel cell is performed. These recomputed clad heights are then used to assess the layer-wise deposition process at the current layer. Consequently, a novel algorithm to localize defects that trail on the surface of the build parts without the need for external hardware has been proposed. After preprocessing, the high-dimensional point cloud data are thoroughly examined to further extract features characterized as defects for process monitoring. Clusters of defects that propagate along the growth direction that may have originated from previous layers and could potentially weaken the quality of the final product are identified using the novel defect-finder algorithm.

1) BATCH RASTERIZATION OF THE UNORDERED POINT CLOUDS AS BENCHMARK OF RASTERIZATION METHOD

The laser head moves along the substrate, leaving behind trails of sampling points following the tool path. Because of the inconsistent sampling rates, these time-dependent tool-path data points may not be equally distributed; therefore, a re-sampling technique is performed to transform the tool-path data points (time-dependent signal) into spatial equidistant sampling points in a 2-D Cartesian plane.

Before describing the proposed real-time rasterization method, a batch-processing approach of rasterization, a widely known technique in the literature [28], [29], [36], [41], [54], [57], [58] is described in this section. The method is used for comparison study and benchmarking purpose with the proposed real-time rasterization method. It is noted that the batch-processing approach can only be used to analyze the deposited layer information upon completion. This contrasts with the proposed real-time rasterization method, which rasterizes the data streams real-time during the deposition as the laser head moves along the pre-defined tool path.

For the pre-processing step, boundaries encompassing the entire structure of the dataset (X_L^{min}, X_L^{max}, Y_L^{min} and Y_L^{max}) are first obtained, where L is the total number of layers. Subsequently, equidistant sampling points are generated in the 2-D coordinate space within the bounds of the structure, separated by k resolution (offset). These equidistant point coordinates are conjoined with their respective bounding boxes and appended to a dictionary, where the point coordinates act as keys while the values ($x-k/2$, $x+k/2$, $y-k/2$ and $y+k/2$) store its bounding box boundary. Furthermore, a re-sampling procedure for each layer by obtaining the X and Y boundaries of the current i^{th} layer l_i ($X_{l_i}^{min}$, $X_{l_i}^{max}$, $Y_{l_i}^{min}$ and $Y_{l_i}^{max}$) layer have been defined, the relevant time-dependent sampling points within a pre-defined size k of the bounding boxes (or pixels) can be congregated. Subsequently, the median or mean of the clad height data was obtained. However, in some cases, the key does not contain any sampling points and, thus, returns a null value. In such cases, a simple data null imputation procedure needs to be performed by creating a padding of size n surrounding the null key offset by a k resolution (3 × 3 window), and then taking the median or mean of the height data on the padding [41]. This median or mean value was used to impute the key with a null value. These re-sampling and null-filling procedures are repeated until all layers are processed.

As an output of the batch rasterization re-sampling approach, consider the re-sampled list D containing a set of re-sampled clad height arrays. The list D contains vectors in the form of $\{X \in \mathbb{R}^M, Y \in \mathbb{R}^N, Z \in \mathbb{R}^L\}$ and a matrix format as $\{\mathbf{H} \in \mathbb{R}^{M \times N \times L}\}$, where X, Y, and Z denote the X, Y, and Z coordinates of the re-sampled points, respectively, and H denotes the clad height data. Notations M, N, and L represent the dimensions of the re-sampled X, Y, Z coordinates, respectively. It is worth noting that the dimension of the Z coordinate is equal to the total number of layers L. The results of this algorithm are used in the subsequent steps.

2) THE PROPOSED REAL-TIME RASTERIZATION OF THE UNORDERED POINT CLOUDS

Although the batch rasterization method can generate equidistant spatial sampling points, it can only be performed

at the end of the layer deposition during the dwell time phase when all the data have been collected. A real-time re-sampling method is needed to provide real-time feedback to the operator and to ensure that the error does not accumulate. A real-time method is also able to retain the temporal aspects of the re-sampled data on top of the spatial aspects; thus making it a spatiotemporal (space-time) method, as shown in Fig. 4. For instance, retaining the temporal information in the real-time rasterization technique, representing the deposition's tool path, may help the researcher to pinpoint any abnormalities found in the re-sampled time-series data, i.e., ordered point cloud with time ordering. This is not possible with the prior batch re-sampling method; consequently, during the aggregation stage, raw data points r_i within the raster cell may contain a number of raw data points separated by a significant difference in timestamps that will be aggregated together, causing tool-path disarray. However, the statistical properties of the data cannot be easily computed in a real-time rasterization method, in contrast to the batch re-sampling method, where all the data have been collected and are already available before processing and analysis. In real-time situations, the deposition tool path is arbitrary. Considering all of the above, an alternative rasterization re-sampling algorithm that can be deployed in real-time has been developed.

A simple and intuitive explanation of this method is presented in Fig. 4. At time t_1, for the first observation or pixel, an artificial box with a boundary offset of $k/2$ resolution surrounding it during the initialization stage is created. In the real-time rasterization, the resolution k is constrained to the 3D printer setup, i.e., hatch spacing of the tool-path. Therefore, resolution k cannot be changed, unlike batch rasterization. Subsequently, in the next time step, there will be at most two possibilities in which the raw data point r_{t+1} either lies within or outside the recently created pixel. In real applications, more than one raw data point may exist within a single pixel. If the next raw data point r_{t+1} lies within the recently created pixel $p_i = \{r_1, r_2, \ldots, r_t$, the mean of the clad height and timestamps of all raw data points belonging to p_i is recomputed to give $p_i(x, y, z, t_i, h_i)$. On the other hand, if r_{t+1} falls outside p_i, then the padding search algorithm is activated, creating a padding (initialize with a 3 × 3 window) offset by k with size n surrounding p_i (refer to Algorithm 1). If it fails to detect within the first padding, the algorithm stacks the additional padding surrounding the previously created padding until the next r_{t+1} is located. In the real-time rasterization process, unobserved or new pixels are iteratively updated to global subdivisions, as shown in Fig. 3b. This procedure is necessary to ensure that all the pixels in the subsequent layers are aligned along the Z-axis, for example, stacking on top of the previous layer pixels. In the case of null imputation of missing pixels during the rasterization technique, instead of creating a 3 × 3 window and taking the median, this method uses 1-D linear interpolation to account for the mixing pixels' values as delineated in Fig. 4. A more comprehensive and detailed explanation of

the real-time rasterization re-sampling method is provided in Algorithm 2.

In contrast to the batch rasterization method, which can only preserve spatial data, the real-time algorithm preserves the spatiotemporal aspects of the data (both space and time). List D contains a mixed set of vectors and matrice as $\left\{X \in R^M, Y \in R^N, Z \in R^L, \mathbf{H} \in R^{M \times N \times L}, \mathbf{T} \in R^{M \times N \times L}\right\}$, where X, Y, and Z denote the X, Y, and Z coordinates of the re-sampled (ordered) point clouds, respectively, T denotes the timestamps of the actual deposition, and H denotes the clad height data. Notations M, N, L represent the dimensions of the re-sampled X, Y, Z coordinates, respectively. The results of this algorithm are used in the scoring evaluation algorithm.

Algorithm 1 Padding Search

1: **Function** $PaddingSearch(p_i(x, y), r_t(x, y), k)$:
2:      $n \leftarrow 0$
3:      $locate \leftarrow 0$
4:      **while** $locate \neq 1$:
5:          $n \leftarrow n + 1$
6:          $d_{pad} \leftarrow$ Create padding with size n
              surrounding $p_i(x, y)$
7:          $X_{pad} \leftarrow$ Get all unique X coordinate from d_{pad}
8:          $Y_{pad} \leftarrow$ Get all unique Y coordinate from d_{pad}
9:          **for** x in X_{pad}:
10:             **for** y in Y_{pad}:
11:                 **if** $(x - k/2 \leq r_t(x) < x + k/2)$
                    and $(y - k/2 \leq r_t(y) < y + k/2)$:
12:                     $locate \leftarrow 1$
13:                     **return** $p_{i+1}(x, y), i+1$
14:             **else:**
15:                 **Continue**
16: **end Function**

---

3) CALCULATIONS OF THE NEW POINT CLOUD HEIGHT

By default, the sensor reads out the new clad height at a particular point in time from the reference plane to the top of the clad geometry. In this study, the vision-based sensor resets the reference plane to zero for every new layer. For instance, from Fig. 5., the original reading of the total height at pixel 2 is 1010, but this is somewhat misleading because of the nature of the vision height camera sensor data acquisition approach, as stated previously.

Since the data structure of the point clouds had been transformed using the proposed real-time rasterization approach, it is possible to re-correct these point clouds' attribute, particularly, their clad height data, such that any under or over-deposition at a particular point is not being compensated. A re-computation is necessary to account for these incorrect measurements during the process using:

$$h_{new}(m, n, l) = [(l - 1) \times \delta + h(m, n, l)]$$
$$- \sum_{j=0}^{l-1} h_{new}(m, n, j) \quad (1)$$

Algorithm 2 Real-Time Rasterization Re-Sampling Method

Input:	Streaming data, $r_t \in \mathbf{R}$
Output:	$p_{glob} = []$
	$D = \{p_1(x, y, h_1), p_2(x, y, h_2), \dots,$
	$p_i(x, y, h_i)\}$

1:    **while** printing a layer
2:      $i \leftarrow 0$
3:      $X_{glob} \leftarrow$ Get all the unique X-coordinate from p_{glob}
4:      $Y_{glob} \leftarrow$ Get all the unique Y-coordinate from p_{glob}
5:      **if** initialize $\neq 1$:
6:        **try:**
7:          $i \leftarrow i + 1$
8:          **if** $(X_{glob} - k/2 \leq r_t(x) < X_{glob} + k/2)$ and $(Y_{glob} - k/2 \leq r_t(y) < Y_{glob} + k/2)$
9:            Initialize $p_i(x, y)$ using the $p_{glob}(x, y)$
10:          **else**
11:            Initialize $p_i(x, y)$ using the $r_t(x, y)$
12:        **except**
13:          Establish $p_i(x, y)$ at the vicinity of any $p_{glob}(x, y)$ offset by k
14:          Append r_t to $p_i(x, y)$
15:          $t_i, h_i \leftarrow$ Get the mean of the timestamps and clad height from $r_t(x, y)$
16:          $p_i(x, y, t_i, h_i) \leftarrow$ Assign t_i, h_t to $p_i(x, y)$
17:          Append $p_i(x, y, t_i, h_i)$ to $\mathbf{D}$
18:      **else**
19:        **if** $(p_i(x) - k/2 \leq r_t(x) < p_i(x) + k/2)$ and $(p_i(y) - k/2 \leq r_t(y) < p_i(y) + k/2)$
20:          Append r_t to $p_i(x, y)$
21:          Re-compute t_i and h_i based on all r in $p_i(x, y)$
22:          Re-assign $p_i(x, y, t_i, h_i)$ from
23:        **else**
24:          $p_i(x, y), i \leftarrow PaddingSearch\ p_i(x, y), r_t(x, y), k()$
25:          Append r_t to $p_i(x, y)$
26:          $t_i, h_i \leftarrow$ Get the mean of the timestamps and clad height from $r_t(x, y)$
27:          $p_i(x, y, t_i, h_i) \leftarrow$ Assign t_i, h_t to $p_i(x, y)$
28:          Append $p_i(x, y, t_i, h_i)$ to $\mathbf{D}$
29:     **if** null pixel(s) exist **then**
30:        Assign h of null pixel(s) using 1-D linear interpolation between the pixels of the null pixel

---

where $h(m, n, l)$ and $h_{new}(m, n, l)$ are the raw and new clad height instances, respectively, at the mth, n^{th}, l^{th} indices of re-sampled point index, where $m \in M$, $n \in N$, and $l \in L$, respectively. The constant δ is the nominal threshold value which corresponds to the machine's setup of z-increment at every layer. Referring back to Fig. 5 together with (1), the height recorrection method involves adding the ideal height, δ, up to the previous layer $l - 1$, to the pixel height indexed at m^{th}, n^{th}, l^{th} of the resampled point and then, deducting the cumulative re-corrected height of the same index point up to

the preceding layer $l - 1$. This process is executed across every pixel within the layer to output the new re-corrected height h_{new}.

It is clear from the equation that the new clad height $h_{new}(m, n, l)$ is not only dependent on the raw clad height deposited in the lth layer, but also the new clad height instances of the previous layers. Consequently, if no action is done at the lth layer to rectify under- or over-deposition, the defect may propagate and even worse, worsen at the subsequent layer.
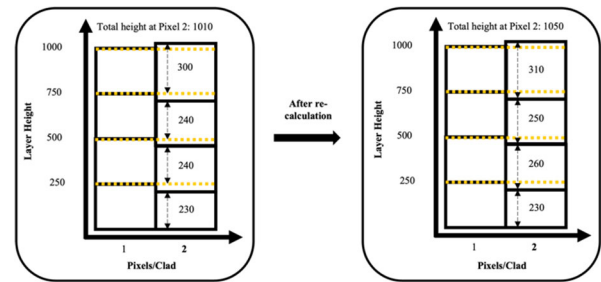

FIGURE 5. An illustration shows before (left) and after (right) re-calculates the raster/voxel height. The orange dashed line indicates the reference layer height.

4) PERFORMANCE EVALUATION

During deposition, variations in clad height h_{new} may be observed within the same layer ($l \in L$), which may be due to the chosen process parameters, including the type of deposition pattern, laser power, powder feed rate, travel speed, and other external disturbances. The percentage deviation between the observed melt-pool height data and the nominal threshold value δ can be used as a performance metric, as shown in Fig. 1c, with percentage deviation $d(m, n, l)$ at the mth, n^{th}, l^{th} indices can be determined:

$$d(m, n, l) = \frac{h_{new}(m, n, l) - \delta}{\delta} \times 100 \qquad (2)$$

where $h_{new}(m, n, l)$ is the re-corrected clad height instance at the mth, n^{th}, l^{th} indices of re-sampled point index of lth layer.

Given that the laser power $p(m, n, l)$ can be used to control the amount of deposition $h(m, n, l)$ at the current layer and that the new clad height $h_{new}(m, n, l)$ is dependent on the new clad height instances of the previous layers, it can be determined that the percentage deviation $d(m, n, l)$ is then dependent on both the laser power and the previous layers' new clad height instances, i.e., $d(m, n, l) = f(p(m, n, l), h_{new}(m, n, i) : i = 1, \dots, l-1)$. The aim of laser power controlled at the lth layer should then be to minimise percentage deviation at that layer l,

$$\min_{p(m, n, l,)} \{d(m, n, l)\}^2 \qquad (3)$$

$$\text{subject to} \quad h_{new}(m, n, i) : i = 1, \dots, l - 1 \qquad (4)$$

Furthermore, $d(m, n, l)$ alone is insufficient to detect any abnormalities. Thus, feature scaling is indispensable to avoid
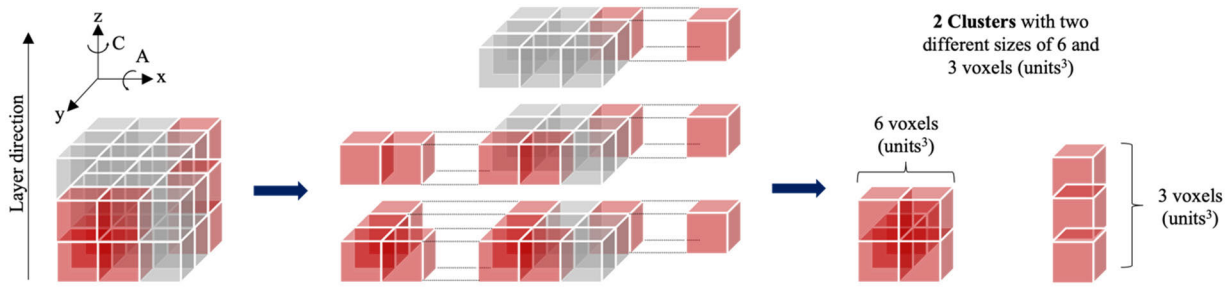
FIGURE 6. The intuitive schematic diagram of the defects-finder algorithm process.

the domination of features with larger or smaller values. A scoring evaluation algorithm can be used to summarize the overall process performance. This study proposed an S-point scoring system, via a 7-point scoring system, $S = \{0, 1, 2, 3, 4, 5, 6, 7\}$, with 0 and 7 indicating the worst and best possible scores, respectively. Subsequently, the assignment of these scores is apportioned to the respective set of intervals Int,

$$Int_s \leftarrow \begin{cases} 100, & s = 0 \\ 100 - \left(s \times \dfrac{100}{|S| - 1}\right), & s > 0 \end{cases} \quad (5)$$

Consequently, each instance $h_{new}(m, n, l)$ is assigned to a score function,

$$score\left(h_{new}(m, n, l)\right) = \begin{cases} 0, & |d(m, n, l)| \geq Int_0 \\ s, & Int_s \leq |d(m, n, l)| < Int_{s-1} \end{cases}$$
$$(6)$$

The generation of layerwise heatmap tomography uses the results containing a set of arrays of scores after computing the re-sampled list D using the abovementioned equations. This heatmap tomography provides insights that reveal spatial defects in the context of geometrical characteristics, that is, under (negative $d(m, n, l)$) and over-deposition (positive $d(m, n, l)$) of the process. The colors are mapped based on set of percentage deviation intervals.

5) DEFECTS-FINDER ALGORITHM
A score of 0 indicates a percentage deviation of over 100% from the nominal value and this strongly suggests the presence of a defect that may induce to larger defects. For the application at hand, the preprocessed point cloud data $P \in R^{i \times j \times k}$ with the assigned scores can be represented based on XYZ voxels within the build coordinate system, as shown in Fig. 6. From the figure, it can be seen that each layer contains red-colored voxel with 0-score. Fig. 6. also shows an example of detected defects constellated into two clusters with different sizes. The central idea of this defects-finder algorithm is based on the recursive function that finds adjacent anomalous voxels (0-score) in 3D space, merging them into individual clusters, as outlined in Algorithms 3-4. Each voxel is marked as not visited in the initialization phase to

avoid repetitive searches at the exact locations. Suppose an anomalous and unvisited voxel is detected by Algorithm 3, then it will count as a cluster root. Then, the *DefectsSize* function (see Algorithm 4) will recursively search by creating a $3 \times 3 \times 3$ cuboids window to search for adjacent anomalous voxels from the initial voxel.

Algorithm 3 Defects-Finder

Input:	Point cloud matrix with scores, $P \in \mathbb{R}^{i \times j \times k}$
	Selected score, s
Output:	Defects cluster, $C : ID \rightarrow (size, coordinates)$,
	where ID is the cluster index

1:    **Function** *Defects-Finder(P, s)*:
2:      $cluster\_count \leftarrow 0$
3:      $visited \in M_{i \times j \times k}(False)$
4:      **for** l in range(i):
5:        **for** y in range(j):
6:          **for** x in range(k):
7:            **if** (P_{ijk}==s) ($visited_{ijk}$==False)**:**
8:              $cluster\_count = cluster\_count + 1$
9:              $cluster\_size =$
                $DefectsSize(P, visited, s, x, y, l)$
10:            Get the cluster coordinates and assign
               to CID along with the $cluster\_size$
11:      **return** C
12:   **end Function**

IV. RESULTS AND DISCUSSION
A. EXPERIMENTAL SETUPS
Most studies in this field have focused mainly on simple structure analysis, such as single- or multi-track and thin-wall structures, despite the fact that objects with complex shapes are commonly fabricated in real-world applications. Quite a few studies have investigated the optimal processing parameters for achieving the maximum inclination angle, such as the type of deposition pattern, z-increment, laser power, scanning speed, and powder feed rate [66], [67], [68], [69], [70]. However, the purpose of this paper is not to achieve that goal. Rather, the objective is to verify the effectiveness of the proposed framework, in which the overhang structure was used as an experiment; since DED can print without

---

Algorithm 4 Determine the size of the clusters

1: **Function** *DefectsSize(P, visited, s, x, y, l):*
2:      **if** $(l < 0)$ **or** $(l \geq i)$ **or** $(y < 0)$ **or** $(y \geq j)$ **or** $(x < 0)$ **or** $(x \geq k)$
        or $(visited_{ijk} == True)$ **or** $(P_{ijk} \neq s)$ **:**
3:          **return** 0
4:      $visited_{ijk} == True$
5:      $cluster\_size = cluster\_size + 1$
6:      **for** l_2 in range$(l - 1, l + 2, 1)$:
7:          **for** y_2 in range$(y - 1, y + 2, 1)$:
8:              **for** x_2 in range$(x - 1, x + 2, 1)$:
9:                  **if** $(l_2, y_2, x_2,) \neq (l, y, x)$ **:**
10                     $cluster\_size +=$
                    $DefectsSize(P, visited, s, x, y, l)$
11:     **return** $cluster\_size$
12: **end Function**

---

a supporting structure [71], avoiding the need for a post-treatment process.

Unlike its counterpart, the SLM process relies on the powder bed that acts as a support structure, simultaneously mitigating thermal warping adjacent to overhanging areas. However, the removal of the additional support structure is often laborious, with an extensive support structure that directly increases post-processing time and costs and inescapably leads to high surface roughness after peeling off the support materials [72]. This experiment was done to ensure the dependability and resilience of the proposed framework by detecting any slight process changes that might lead to significant surface flaws.

Consequently, overhang structures with inclination angles ranging from 0 to 10° were used for evaluation purposes. These experiments were tested using real experimental data generated from the DLMF DMX 01 (Hwacheon Machinery Co., Ltd, South Korea), as depicted in Fig. 1. Powder of Inconel 718, a nickel alloy manufactured by Sandvik with a size range of 53-150 μm, has been selected due to its industrial relevance, in particular for the aerospace industry [73]. The substrate material used for the experiments was a 20 mm thick stainless steel (S45C) sheet. Each structure was first constructed at an inclined angle of 0° up to 10 mm in height, upon which a slope of N° was deposited. The total height of all the structures was 30 mm. The process parameters included a z-increment of 0.25 mm, scanning speed of 850 mm/min, powder feed rate of 4.5 g/min, and coaxial gas flow rate of 6.8 l/min. The laser power was adjusted based on the closed-loop control strategy, according to the melt-pool height. The filling deposition pattern was zigzag with a tool spacing of 0.5 mm. Additionally, the *k* resolution used in this study was 0.5 mm. To enhance the geometrical accuracy of the manufactured part, a double-contour scanning strategy was deployed for this experiment, that is, contour-filling-contour.

Fig. 7. shows the results for the overhang structure. The purpose of the experiment was to correlate and verify the physical defects that can be clearly observed on the edges and surfaces of the structure with the results from the proposed method.

The experiments were conducted on a MacBook M1 Pro 2021 with 16 GB RAM, using Python 3.9. Several preprocessing steps were required to separate the printing mode (contours and filling) using the laser power values as an indicator. When the laser head moved to a new position after finishing a print of either the contour or filling mode, the laser was turned off during this process. Thus, both the reading value of the laser from the system and the vision height sensor value would be zero. As such, this laser-off period indicates the transition phase from one mode to another. Because the deposition process is sequential, that is, contour-filling-contour, they can be easily identified based on the sequence (first contour, laser-off, filling, laser-off, and second contour). As part of data preprocessing, the time-series data of the laser-off period were removed, keeping only the important information, as shown in Fig. 8. For data visualization, the focus was only on the filling mode. Moreover, the layers were separated based on the Z-axis coordinate of the laser head. As mentioned previously, a z-increment of 0.25 mm was used in the experiment, with every increment indicating that a new layer was established.
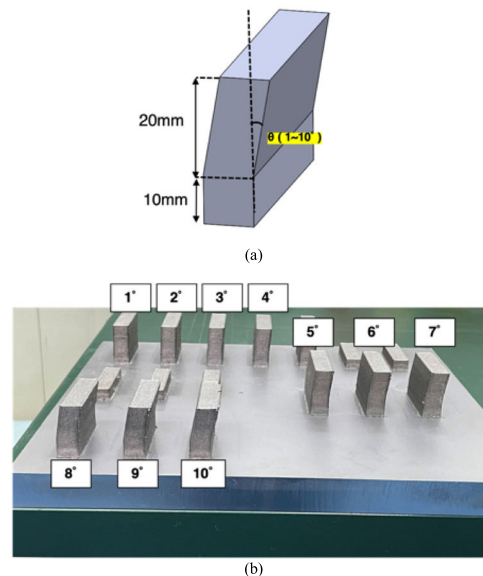

FIGURE 7. (a) Physical artifacts of the printed parts ranging from 0 to 10°; (b) 3D CAD Overhang Model.

B. ALGORITHM EFFECTIVENESS

As previously discussed, the main drawback of near real-time batch processing is that it causes tool path discontinuities as it aggregates data points from different timestamps, particularly when the resolution is large. On the other hand, if the resolution is small, there will be many pixels without the timestamp
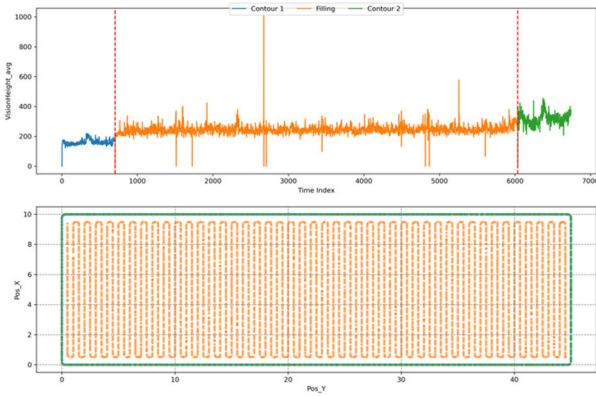
FIGURE 8. Preprocessed time series of the vision height sensor values and the deposition toolpath visualization of one of the layers.

Angle	MSE
0°	0.9999 ± 0.4051
1°	2.9427
2°	6.0768
3°	5.6142
4°	3.9838
5°	4.6994
6°	3.6676
7°	29.6588
8°	11.6392
9°	10.8212
10°	42.4962
Average	12.16

attribute. Assigning a timestamp t to these pixels alters the original toolpath with a smaller hatch spacing. These are the main problems encountered when batch processing with different resolutions is performed.

As previously discussed, the real-time rasterization approach can only achieve a resolution $k = 0.5$ mm bounded by the tool-path's hatch spacing during the initialization of the 3D printer setups. Nevertheless, this method preserves temporal and spatial information, including tool-path deposition in the Cartesian space and its trajectories, which benefits researchers in detecting abnormalities and mapping coordinates back to the timestamps for further analysis. On the other hand, the batch rasterization method has more flexibility in changing the resolution k but loses temporal information. Therefore, there is a trade-off between choosing a finer or coarser resolution k or a fixed resolution k bound with the hatch spacing but retaining tool-path trajectories.

To compare batch (near-real-time) and real-time processing methods for the rasterization process, it is necessary to quantitatively measure the differences between them for validation purposes, with the Mean Squared Error (MSE) used for this purpose. As both methods use the same data structure and coordinates, comparing the computed height data pixel-by-pixel is possible. The closer the value is to zero, the more accurate the real-time method is to the batch rasterization method.

$$MSE = \frac{1}{P} \sum_{m=0}^{M} \sum_{n=0}^{N} \sum_{l=0}^{L} \left[h_{new}^{b}(m, n, l) - h_{new}^{r}(m, n, l) \right]^2 \quad (7)$$

where P is the total pixels, h_{new}^{b} and h_{new}^{r} represent batch and real-time pixel heights, respectively, and both are indexed at the same m^{th}, n^{th}, l^{th} re-sampled point for comparisons, where $m \in M$, $n \in N$, and $l \in L$, respectively. Small MSE suggests small variation between the benchmark re-sampling method (batch) and the proposed method (real-time).

A validation summary of the real-time and batch rasterization approaches is tabulated in Table 1. These variations exist between the two methods because of the different re-sampling methods, specifically in the null imputation process. Batch

rasterization infers a null value based on the mean or median of neighboring pixels. Meanwhile, real-time rasterization uses interpolation between two re-sampled data points of the null value. The lowest (0.9999) and highest (42.4962) MSEs occurred at 0° and 10° inclination angles, respectively. The average MSE for all the inclination angles was 12.16. In addition, the MSE of the 7° inclination angle is relatively high compared to 6° and 8°, and the possible reasons for this high error may be caused by (1) the aforementioned null value imputation differences; if the neighboring values are too high, the null value inference is also high, thus inducing high errors for the respective pixels and (2) human error or other related external factors during the deposition process may cause the quality to degrade, resulting in high deviations, and subsequently affect the reasoning mentioned above. In this study, the batch processing uses the median operator with a 3×3 window to compute the missing measurement pixels [41]. Meanwhile, our proposed method, uses the interpolation between the ordered point clouds to deal with missing pixels/raster cells. One way to circumvent this problem is to replicate the experiments with the same parameters (similar to the case of 0° with ten different samples), average the MSEs of each inclination angle of different samples, and consider the uncertainties between the experiments.

C. STATISTICAL MEASURES AND ANALYSIS AT THE LAYER LEVEL

Visualizing the most important features in two-dimensional space is vital for observing meaningful patterns that are usually difficult to identify in raw sensor readings. In accordance with the present results, correlations between the physical defects and the proposed method are possible by producing a heatmap tomography of the layer. Fig. 9 depicts the results of the batch and real-time re-sampling algorithms for one of the layers in a 10° structure. Additionally, based on these two figures, the real-time algorithm has visually similar results, as validated by the batch processing algorithm.

Moreover, it appears that an inclined angle of 10° has several faults, for example, dark blue at the inflection points, indicating that this particular layer experienced under- deposition below −100%. This particular fault was verified by
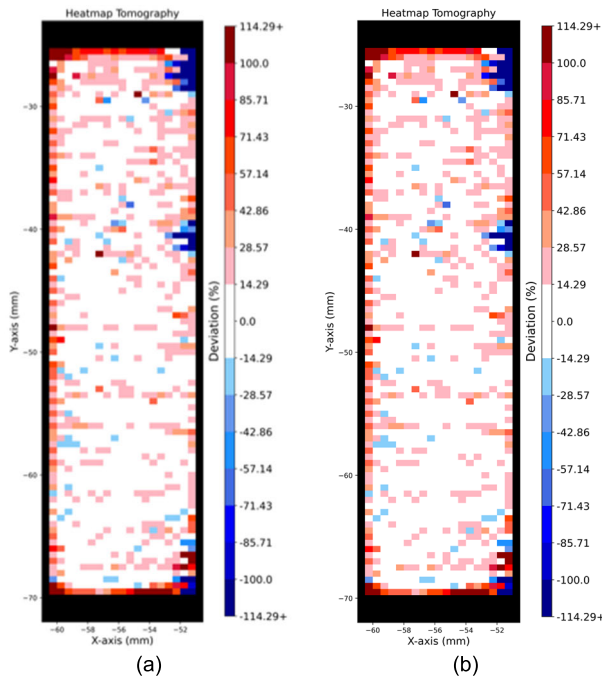
FIGURE 9. Results of (a) batch and (b) real-time rasterization methods at 29.5 mm layer of a 10° structure.

comparing it with the defects in the physical structure, as shown in Fig. 10. The proposed methods, either batch or real-time approach, imitate X-ray computed tomography (CT) functionality, which is widely used in the dimensional measurement of the inner and outer geometries of manufactured parts. Evidently, the proposed method also provides vital information during the process, allowing for profiling the internal structure of the component using 1D time-series data, that is, clad height. However, implementing CT scans for in-situ monitoring results in a slower building process.

A score between 0 to 7 describes the summary performance of the deposition layer based on the corresponding statistical measures. The overall score ratio in this example is the sum of all computed scores divided by the sum of all the maximum scores for that layer. It is apparent from Table 2 that the layer performance at an inclination angle of 1° outperforms that at 10°. This poor performance occurs because some of the regions at 10° are left unsupported by the previous layer; thus, an inclined angle of 10° is more prone to defects.

The results from this table present several important insights. First, all three inclined angles had the same median value, which is not surprising as the median is robust to outliers or extreme values; hence, the median may not be suitable for evaluation. Second, the mean for the inclined angle of 1° was slightly higher than that of 5° and 10°. At layer 111, mean values are 6.478 ± 0.040, 6.300 ± 0.049, and 6.137 ± 0.070, for 1°, 5° and 10°, respectively. From the mean of the three different angles, 10° had the lowest mean compared to the rest, but the difference was not significant. The mean for the inclined angle of 10° indicates that the process was still

good despite the fact that there were critical faults in the layer, as depicted in Fig. 10. This poor representation was similar to the overall score statistic.

Interestingly, the percentile emerged as a better way to assess performance. The 10th percentile of an inclined angle of 1° in layer 111 is 6 points, indicating that over 90% of the total re-sampled points scored above 6 points, and less than 10% scored less. However, the 10th percentile for the 10° inclination angle indicates that less than 10% of the total re-sampled points contain 5 points and below, which is slightly lower than the 1° angle. In addition, the 5th percentile of an inclined angle of 10° is 3 points, indicating that 5% of the total data scores 3 points, while the 1° layer scores 2 points higher. As for the 1st percentile of the 10° angle, it scores 0 points, which 1% of the total re-sampled points of that layer contain bad scores, including extreme over- or under-deposition of more than 100% than the nominal value. This outcome can also be observed in layer 101 of the 10° angle.

As the laser head deposits the material layer by layer, the process may be susceptible to inheriting defects from previous layers containing severe prints, even in a small area. From Table 2, the 1° structure reports almost consistent performance at the 1st percentile, with scores of 3, 3, 4, 3, and 4, at layers 41, 61, 81, 101, and 111, respectively. For the 5° structure, at layers 61 and 101, the 1st percentile scores 1 and 0 points, respectively, indicating that defects start to occur. Meanwhile, the 10° structure reported poor indicators starting from layer 61 and persistently did not improve further.

This statistical property (percentile) provides an early indication of the alarming situation during the deposition process in real-time, even with multiple small defects in the layer. This situation is often true in real applications; as the product is fabricated layer-by-layer, a small detrimental defect could propagate as the layer grows, as illustrated in Fig. 10. and Fig. 11b, which could lead to severe defects.

D. SURFACE DEFECTS CLUSTERS RETRIEVED VIA DEFECTS-FINDER ALGORITHM

In Fig. 12, the Defects-Finder algorithm's results are displayed, showcasing twelve unique clusters that represent surface defects that occurred during the DLMF process. Only collections of surface defects with a size of 10 voxels or more were shown, as the focus was to detect the clusters of surface defects. These defects were validated by visually inspecting the physical artifact of the 10° overhang structure, as shown in Fig. 13a-d. One of the challenges found in this study is to confirm defects with linear horizontal patterns among them, as illustrated in Fig. 12a; upon checking the Fig. 13c-d, based on the eyeballing test, the surface roughness on that particular sides is found to be slightly rough (e.g., white frizzy trails). However, it is difficult to correlate these directly, and the algorithm did not pick this up as a significant cluster defect as preset earlier.

However, Fig. 12b highlights the atrocious surface defects that were picked up by the algorithm, indicated by clusters
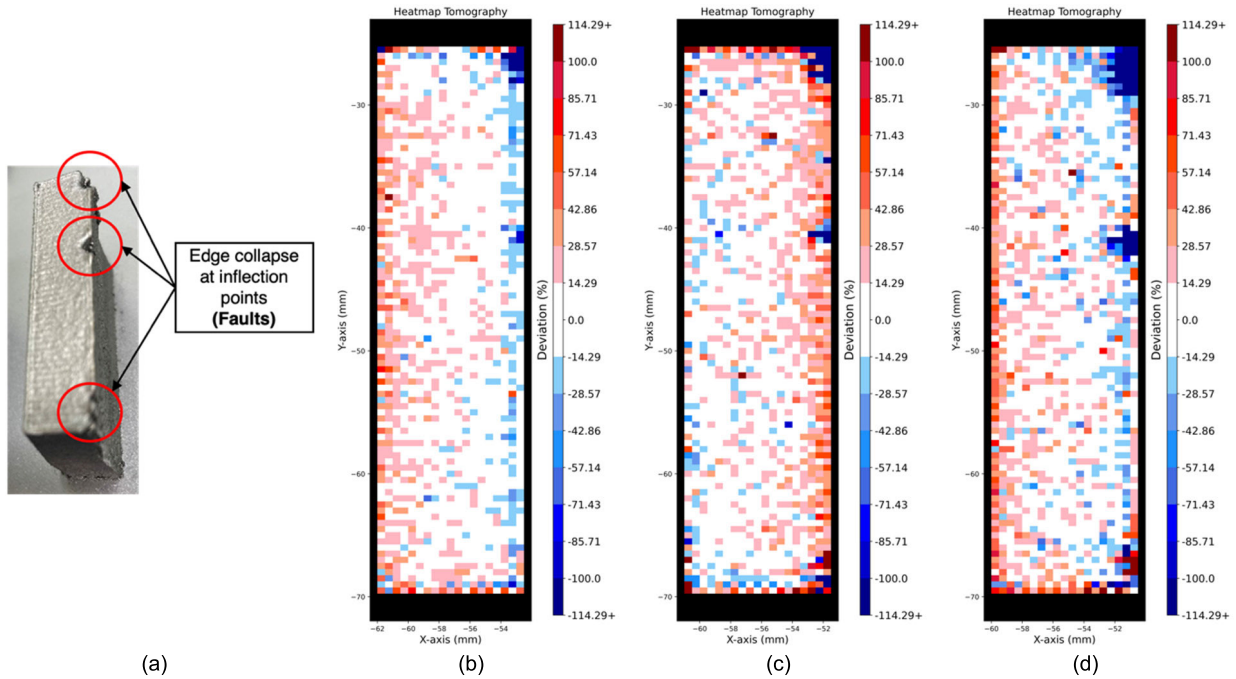
FIGURE 10. A side-by-side comparison between the physical structure and the proposed method; (a) Physical structure of an inclined angle of 10° shows the edge collapse defects at the inflection points; The proposed method heatmap tomography at a (b) layer of 19.5 mm, (c) layer of 24.5 mm, and (d) layer of 30.0 mm.
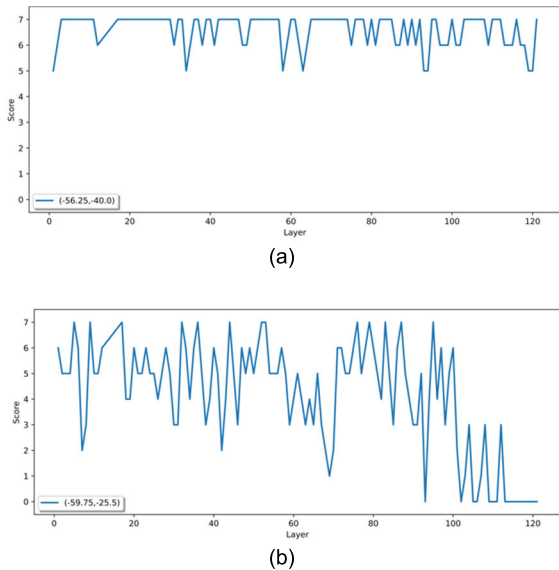

FIGURE 11. The layer-wise score of (a) the normal pixel at coordinate (−56.25, −40) and (b) the degradation of a pixel at coordinate (−59.75, −25.5) of the 10° structure.

ID#{320, 243, 223, 126, 331, 241, 211, 137}. These defects were apparent based on the eyeballing test and can be referenced in Fig. 12b. The most exciting aspect of Fig. 12c is that it delineates the root cause of each cluster and the layer it originated from, and until which layer it ends. This result is tabulated in Table 3. Cluster ID#211 is the largest cluster

amongst all, with a size of 539 voxels, originating from layer 77 up to the final layer. The second largest cluster, ID#320, is disjointed from other smaller clusters with ID#{243, 223} and spans from layer 100 until the last layer with a size of 220 voxels. It is clear that these defects propagate as the layer grows. Based on the results, it can be confirmed that the geometrical characteristics of the clad height are somewhat correlated to surface defects. This is similar to Tang et al. [16] which asserted that the surface quality is pertinent to the geometrical process signatures. Finally, clusters with ID#{294, 102, 128, 239} do not result in severe defects. However, they cause an accumulation of over-deposition at the frontal inflection points or edges, displaying pointy edges, which can be easily observed through visual inspection.

According to the expertise of domain specialists [74], parts with a maximum pore size below 97.10 μm meet expectations and are designated as "pass" parts. Parts with a maximum pore size between 97.10 μm and 220.40 μm fall within a margin area and are labeled as "flag" parts. Parts with a maximum pore size exceeding 220.40 μm are considered "failed" parts. In this study, the voxel size is $500 \times 500 \times 250$ μm, which may be potentially classified as "failed" parts. An investigation into the correlation between internal defects, such as porosities or keyholes, and internal disjointed voxels is rather interesting and should be explored in the future. With the aid of the X-ray CT scan equipment serves as a reliable source of ground truth and should be utilized to confirm any potential correlations derived from the proposed algorithm.
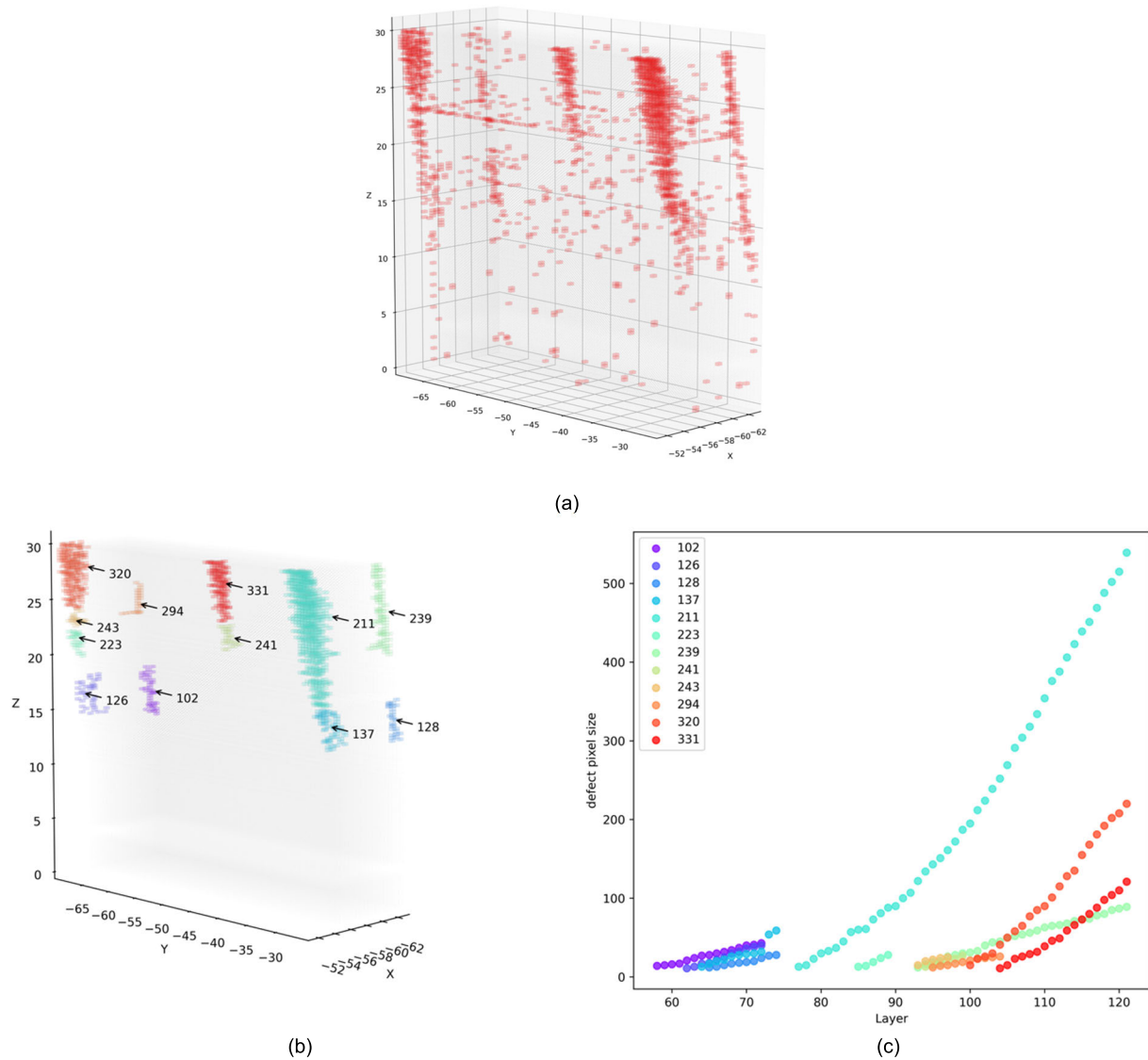
(a)

(b)

(c)

FIGURE 12. (a) Unfiltered voxels with 0-score (red in colour), (b) The clusters of surface defects detected by the Defects-Finder algorithm, (c) A scatterplot that shows the clusters' growth size as layer increases.

(a)

(b)

(c)

(d)
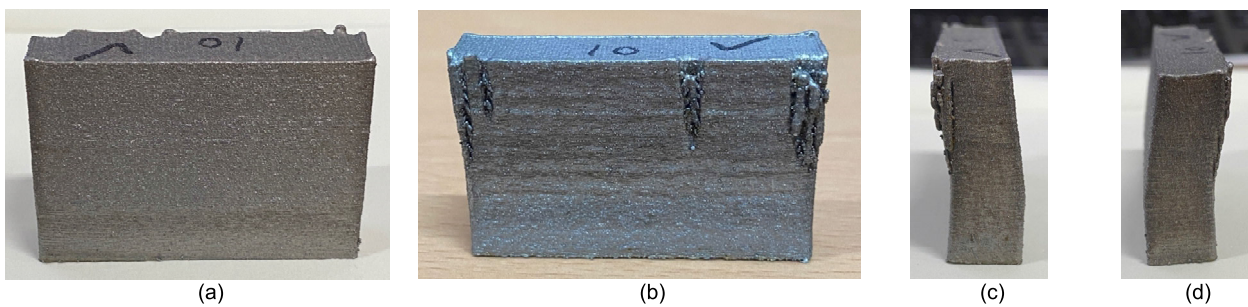
FIGURE 13. Physical artifact of a 10° overhang structure: (a) Front view, (b) Back view, (c) Right-side view, (d) Left-side view.

In the future, it would be interesting to use artificial intelligence (AI) techniques to provide an early indication of failures in advance [75], [76], [77]. For instance, prediction of the anticipated future layers in the subsequent successive layers so that the operator or AI could make necessary adjustments to the reference sets of process parameters. This

TABLE 2. Statistical performance results between three different inclination angles of the layer-level comparison.

Layer	Angle	Overall Score ratio	Mean ± 95% CI	Median	1st percentile	5th percentile	10th percentile
41 (10.0 mm)	1°	0.914	6.400 ± 0.043	7	3	5	5
	5°	0.924	6.465 ± 0.042	7	3	5	5
	10°	0.918	6.424 ± 0.045	7	3	5	5
61 (15.0 mm)	1°	0.919	6.434 ± 0.042	7	3	5	5
	5°	0.893	6.253 ± 0.058	7	1	4	5
	10°	0.889	6.225 ± 0.058	7	1	4	5
81 (20.0 mm)	1°	0.933	6.529 ± 0.036	7	4	5	6
	5°	0.894	6.260 ± 0.050	7	2	4	5
	10°	0.894	6.261 ± 0.051	7	2	4	5
101 (25.0 mm)	1°	0.913	6.389 ± 0.046	7	3	5	5
	5°	0.893	6.251 ± 0.059	7	0	4	5
	10°	0.889	6.225 ± 0.067	7	0	3	5
111 (27.5 mm)	1°	0.925	6.478 ± 0.040	7	4	5	6
	5°	0.900	6.300 ± 0.049	7	3	4	5
	10°	0.877	6.137 ± 0.070	7	0	3	5

TABLE 3. The results of the Defects-Finder algorithm display the ID of each cluster along with its size and the starting and ending layers of its growth.

Cluster #ID	102	126	128	137	211	223	239	241	243	294	320	331
Cluster size (no. of voxels)	43	40	28	59	539	28	89	27	25	26	220	121
Start at Layer	58	62	65	64	77	85	93	94	93	95	100	104
End at Layer	72	72	74	74	121	89	121	99	97	104	121	121

advancement could help decrease the lead time and cost related to post-processing approaches, i.e., rectifying the failed printed components.

V. CONCLUSION

To ensure fabricated parts meet the required specifications, it is crucial to monitor the manufacturing process and understand the variables that can lead to deviations. Fortunately, the layer-by-layer nature of additive manufacturing allows for insights into each layer's topography, such as geometry and potential of over or under-deposition, which play a critical role in quality control. A Defects-Finder approach as a real-time rasterization method capable of locating anomalous agglomerated voxels without the need for external hardware or post-processing, has been proposed in this paper. The proposed method rasterizes the incoming data streams in real-time, generating structured point cloud data with spatial-temporal information. This is in contrast to the near-real-time state-of-the-art technologies of rasterization method, which when combined with need of inter-layer inspection, can drastically increase inter-dwelling times. Therefore, this advancement in point cloud processing, together with the downstream analysis—Defects-Finder—is a remarkable improvement in metal AM; improving the manufacturing lead time and

foregoing the need of post-processing. Overhang structures ranging from 0° to 10° were used to validate the proposed method. The study demonstrates that the algorithm effectively localizes faults in the deposition process on the layer. Several statistical properties were employed to evaluate the performance at a layer level, providing insights into which properties better represent the overall performance—notably, increasing the inclination angle adversely impacted performance. In layer 111 of a 10° slope structure, the overall score, mean, and median were 0.877, 6.137, and 7, respectively. These values were deemed high, erroneously indicating that the deposition process of that layer was good, considering a scoring scheme with a maximum value of 7. However, the 1st, 5th, and 10th percentiles were 0, 3, and 5, respectively; making the percentile the best measure for guaranteeing abnormality detection in the imbalance classification problem, as it quantified the number of non-zero points, which other statistical measures failed to do.

Subsequently, this study paves the way for an alternative to quality control in AM and a closed-loop control strategy to compensate for faults/errors found within the vicinity. In the future, expert domain knowledge can aid in labeling anomalous presence in the layer for further analysis, such as defects classification based on Convolutional Neural Networks.

REFERENCES

[1] T. Pereira, J. V. Kennedy, and J. Potgieter, "A comparison of traditional manufacturing vs additive manufacturing, the best method for the job," *Proc. Manuf.*, vol. 30, pp. 11–18, Jan. 2019.

[2] P. R. Gradl, O. R. Mireles, C. S. Protz, and C. P. Garcia, *Metal Additive Manufacturing for Propulsion Applications*. American Institute of Aeronautics and Astronautics, 2022, doi: 10.2514/4.106279.

[3] B. Blakey-Milner, P. Gradl, G. Snedden, M. Brooks, J. Pitot, E. Lopez, M. Leary, F. Berto, and A. Du Plessis, "Metal additive manufacturing in aerospace: A review," *Mater. Des.*, vol. 209, Nov. 2021, Art. no. 110008.

[4] A. Vafadar, F. Guzzomi, A. Rassau, and K. Hayward, "Advances in metal additive manufacturing: A review of common processes, industrial applications, and current challenges," *Appl. Sci.*, vol. 11, no. 3, p. 1213, Jan. 2021.

[5] C. Schneider-Maunoury, L. Weiss, P. Acquier, D. Boisselier, and P. Laheurte, "Functionally graded Ti6Al4V-Mo alloy manufactured with DED-CLAD process," *Additive Manuf.*, vol. 17, pp. 55–66, Oct. 2017.

[6] T. D. Ngo, A. Kashani, G. Imbalzano, K. T. Q. Nguyen, and D. Hui, "Additive manufacturing (3D printing): A review of materials, methods, applications and challenges," *Compos. B, Eng.*, vol. 143, pp. 172–196, Jun. 2018.

[7] A. Gaikwad, R. Yavari, M. Montazeri, K. Cole, L. Bian, and P. Rao, "Toward the digital twin of additive manufacturing: Integrating thermal simulations, sensing, and analytics to detect process faults," *IISE Trans.*, vol. 52, no. 11, pp. 1204–1217, Nov. 2020.

[8] M. Liu, A. Kumar, S. Bukkapatnam, and M. Kuttolamadom, "A review of the anomalies in directed energy deposition (DED) processes & potential solutions—Part quality & defects," *Proc. Manuf.*, vol. 53, pp. 507–518, Jan. 2021.

[9] Z. Chen, C. Han, M. Gao, S. Y. Kandukuri, and K. Zhou, "A review on qualification and certification for metal additive manufacturing," *Virtual Phys. Prototyping*, vol. 17, no. 2, pp. 382–405, Apr. 2022.

[10] P. R. Sreeraj, S. K. Mishra, and P. K. Singh, "A review on non-destructive evaluation and characterization of additively manufactured components," *Prog. Additive Manuf.*, vol. 7, no. 2, pp. 225–248, Apr. 2022.

[11] H. Kim, Y. R. Lin, and T. L. B. Tseng, "A review on quality control in additive manufacturing," *Rapid Prototyping J.*, vol. 24, no. 3, pp. 645–669, Apr. 2018.

[12] S. Pratheesh Kumar, S. Elangovan, R. Mohanraj, and J. R. Ramakrishna, "Review on the evolution and technology of state-of-the-art metal additive manufacturing processes," *Mater. Today, Proc.*, vol. 46, pp. 7907–7920, Jan. 2021.

[13] M. Armstrong, H. Mehrabi, and N. Naveed, "An overview of modern metal additive manufacturing technology," *J. Manuf. Processes*, vol. 84, pp. 1001–1029, Dec. 2022.

[14] K. Vartanian and T. McDonald, "Accelerating industrial adoption of metal additive manufacturing technology," *JOM*, vol. 68, no. 3, pp. 806–810, Mar. 2016.

[15] M. Schmidt, M. Merklein, D. Bourell, D. Dimitrov, T. Hausotte, K. Wegener, L. Overmeyer, F. Vollertsen, and G. N. Levy, "Laser based additive manufacturing in industry and academia," *CIRP Ann.*, vol. 66, no. 2, pp. 561–583, 2017.

[16] Z.-J. Tang, W.-W. Liu, Y.-W. Wang, K. M. Saleheen, Z.-C. Liu, S.-T. Peng, Z. Zhang, and H.-C. Zhang, "A review on in situ monitoring technology for directed energy deposition of metals," *Int. J. Adv. Manuf. Technol.*, vol. 108, nos. 11–12, pp. 3437–3463, Jun. 2020.

[17] S. K. Everton, M. Hirsch, P. Stravroulakis, R. K. Leach, and A. T. Clare, "Review of in-situ process monitoring and in-situ metrology for metal additive manufacturing," *Mater. Des.*, vol. 95, pp. 431–445, Apr. 2016.

[18] M. Grasso and B. M. Colosimo, "Process defects and in situ monitoring methods in metal powder bed fusion: A review," *Meas. Sci. Technol.*, vol. 28, no. 4, Apr. 2017, Art. no. 044005.

[19] R. K. Leach, D. Bourell, S. Carmignato, A. Donmez, N. Senin, and W. Dewulf, "Geometrical metrology for metal additive manufacturing," *CIRP Ann.*, vol. 68, no. 2, pp. 677–700, 2019.

[20] K. Bi, D. Lin, Y. Liao, C.-H. Wu, and P. Parandoush, "Additive manufacturing embraces big data," *Prog. Additive Manuf.*, vol. 6, no. 2, pp. 181–197, May 2021.

[21] L. Wang and C. A. Alexander, "Additive manufacturing and big data," *Int. J. Math., Eng. Manag. Sci.*, vol. 1, no. 3, p. 107, 2016.

[22] D. Mies, W. Marsden, and S. Warde, "Overview of additive manufacturing informatics: 'A digital thread,'" *Integrating Mater. Manuf. Innov.*, vol. 5, no. 1, pp. 114–142, Dec. 2016.

[23] R. Kannan, G. L. Knapp, P. Nandwana, R. Dehoff, A. Plotkowski, B. Stump, Y. Yang, and V. Paquit, "Data mining and visualization of high-dimensional ICME data for additive manufacturing," *Integrating Mater. Manuf. Innov.*, vol. 11, no. 1, pp. 57–70, Mar. 2022.

[24] B. Shneiderman, "The eyes have it: A task by data type taxonomy for information visualizations," in *Proc. IEEE Symp. Vis. Lang.*, Sep. 1996, pp. 336–343.

[25] J. Posada, C. Toro, I. Barandiaran, D. Oyarzun, D. Stricker, R. de Amicis, E. B. Pinto, P. Eisert, J. Döllner, and I. Vallarino, "Visual computing as a key enabling technology for Industrie 4.0 and industrial internet," *IEEE Comput. Graph. Appl.*, vol. 35, no. 2, pp. 26–40, Mar. 2015.

[26] M. M. Imran, G. Jung, Y. Kim, P. E. Abas, L. C. De Silva, and Y. B. Kim, "A computational method for improving the data acquisition process in the laser metal deposition," in *Proc. 57th Annu. Conf. Inf. Sci. Syst. (CISS)*, Mar. 2023, pp. 1–6.

[27] M. Grasso, F. Gallina, and B. M. Colosimo, "Data fusion methods for statistical process monitoring and quality characterization in metal additive manufacturing," *Proc. CIRP*, vol. 75, pp. 103–107, Jan. 2018.

[28] Z. Ye, C. Liu, W. Tian, and C. Kan, "In-situ point cloud fusion for layer-wise monitoring of additive manufacturing," *J. Manuf. Syst.*, vol. 61, pp. 210–222, Oct. 2021.

[29] S. P. Donegan, E. J. Schwalbach, and M. A. Groeber, "Multimodal registration and fusion of in situ and ex situ metal additive manufacturing data," *JOM*, vol. 73, no. 11, pp. 3250–3262, Nov. 2021.

[30] Y. AbouelNour and N. Gupta, "In-situ monitoring of sub-surface and internal defects in additive manufacturing: A review," *Mater. Des.*, vol. 222, Oct. 2022, Art. no. 111063.

[31] S. Nasiri and M. R. Khosravani, "Applications of data-driven approaches in prediction of fatigue and fracture," *Mater. Today Commun.*, vol. 33, Dec. 2022, Art. no. 104437.

[32] W. E. Frazier, "Metal additive manufacturing: A review," *J. Mater. Eng. Perform.*, vol. 23, no. 6, pp. 1917–1928, 2014.

[33] C. Wang, X. P. Tan, S. B. Tor, and C. S. Lim, "Machine learning in additive manufacturing: State-of-the-art and perspectives," *Additive Manuf.*, vol. 36, Dec. 2020, Art. no. 101538.

[34] X. Qi, G. Chen, Y. Li, X. Cheng, and C. Li, "Applying neural-network-based machine learning to additive manufacturing: Current applications, challenges, and future perspectives," *Engineering*, vol. 5, no. 4, pp. 721–729, Aug. 2019.

[35] C. Xia, Z. Pan, J. Polden, H. Li, Y. Xu, S. Chen, and Y. Zhang, "A review on wire arc additive manufacturing: Monitoring, control and a framework of automated system," *J. Manuf. Syst.*, vol. 57, pp. 31–45, Oct. 2020.

[36] W. Lin, H. Shen, J. Fu, and S. Wu, "Online quality monitoring in material extrusion additive manufacturing processes based on laser scanning technology," *Precis. Eng.*, vol. 60, pp. 76–84, Nov. 2019.

[37] H. Borovkov, A. G. de la Yedra, X. Zurutuza, X. Angulo, P. Alvarez, J. C. Pereira, and F. Cortes, "In-line height measurement technique for directed energy deposition processes," *J. Manuf. Mater. Process.*, vol. 5, no. 3, p. 85, Aug. 2021.

[38] A. Heralic, A.-K. Christiansson, and B. Lennartson, "Height control of laser metal-wire deposition based on iterative learning control and 3D scanning," *Opt. Lasers Eng.*, vol. 50, no. 9, pp. 1230–1241, Sep. 2012.

[39] M. Faes, W. Abbeloos, F. Vogeler, H. Valkenaers, K. Coppens, T. Goedemé, and E. Ferraris, "Process monitoring of extrusion based 3D printing via laser scanning," 2016, *arXiv:1612.02219*.

[40] S. Donadello, M. Motta, A. G. Demir, and B. Previtali, "Monitoring of laser metal deposition height by means of coaxial laser triangulation," *Opt. Lasers Eng.*, vol. 112, pp. 136–144, Jan. 2019.

[41] J. Lyu and S. Manoochehri, "Online convolutional neural network-based anomaly detection and quality control for fused filament fabrication process," *Virtual Phys. Prototyping*, vol. 16, no. 2, pp. 160–177, Mar. 2021.

[42] E. Binega, L. Yang, H. Sohn, and J. C. P. Cheng, "Online geometry monitoring during directed energy deposition additive manufacturing using laser line scanning," *Precis. Eng.*, vol. 73, pp. 104–114, Jan. 2022.

[43] H.-W. Hsu, Y.-L. Lo, and M.-H. Lee, "Vision-based inspection system for cladding height measurement in Direct Energy Deposition (DED)," *Additive Manuf.*, vol. 27, pp. 372–378, May 2019.

[44] Y. Cheng and M. A. Jafari, "Vision-based online process control in manufacturing applications," *IEEE Trans. Autom. Sci. Eng.*, vol. 5, no. 1, pp. 140–153, Jan. 2008.

[45] C. Gobert, E. W. Reutzel, J. Petrich, A. R. Nassar, and S. Phoha, "Application of supervised machine learning for defect detection during metallic powder bed fusion additive manufacturing using high resolution imaging," *Additive Manuf.*, vol. 21, pp. 517–528, May 2018.

[46] L. Song, V. Bagavath-Singh, B. Dutta, and J. Mazumder, "Control of melt pool temperature and deposition height during direct metal deposition process," *Int. J. Adv. Manuf. Technol.*, vol. 58, nos. 1–4, pp. 247–256, Jan. 2012.

[47] A. Mozaffari, A. Fathi, A. Khajepour, and E. Toyserkani, "Optimal design of laser solid freeform fabrication system and real-time prediction of melt pool geometry using intelligent evolutionary algorithms," *Appl. Soft Comput.*, vol. 13, no. 3, pp. 1505–1519, Mar. 2013.

[48] S. Maffia, V. Furlan, and B. Previtali, "Coaxial and synchronous monitoring of molten pool height, area, and temperature in laser metal deposition," *Opt. Laser Technol.*, vol. 163, Aug. 2023, Art. no. 109395.

[49] H. Kalami and J. Urbanic, "Exploration of surface roughness measurement solutions for additive manufactured components built by multi-axis tool paths," *Additive Manuf.*, vol. 38, Feb. 2021, Art. no. 101822.

[50] J. Akhavan, J. Lyu, and S. Manoochehri, "A deep learning solution for real-time quality assessment and control in additive manufacturing using point cloud data," *J. Intell. Manuf.*, pp. 1–18, Apr. 2023, doi: 10.1007/s10845-023-02121-4.

[51] J. Xiong, Y. Liu, and Z. Yin, "Passive vision measurement for robust reconstruction of molten pool in wire and arc additive manufacturing," *Measurement*, vol. 153, Mar. 2020, Art. no. 107407.

[52] Z. Li, X. Liu, S. Wen, P. He, K. Zhong, Q. Wei, Y. Shi, and S. Liu, "In situ 3D monitoring of geometric signatures in the powder-bed-fusion additive manufacturing process via vision sensing methods," *Sensors*, vol. 18, no. 4, p. 1180, Apr. 2018.

[53] Z. Y. Chua, I. H. Ahn, and S. K. Moon, "Process monitoring and inspection systems in metal additive manufacturing: Status and applications," *Int. J. Precis. Eng. Manuf.-Green Technol.*, vol. 4, no. 2, pp. 235–245, Apr. 2017.

[54] E. T. Lee, Z. Fan, and B. Sencer, "A new approach to detect surface defects from 3D point cloud data with surface normal Gabor filter (SNGF)," *J. Manuf. Processes*, vol. 92, pp. 196–205, Apr. 2023.

[55] R. B. Rusu and S. Cousins, "3D is here: Point cloud library (PCL)," in *Proc. IEEE Int. Conf. Robot. Autom.*, May 2011, pp. 1–4.

[56] R. Schnabel, R. Wahl, and R. Klein, "Efficient RANSAC for point-cloud shape detection," *Comput. Graph. Forum*, vol. 26, no. 2, pp. 214–226, Jun. 2007.

[57] Z. Ye, C. Liu, W. Tian, and C. Kan, "A deep learning approach for the identification of small process shifts in additive manufacturing using 3D point clouds," *Proc. Manuf.*, vol. 48, pp. 770–775, Jan. 2020.

[58] J. Petrich, Z. Snow, D. Corbin, and E. W. Reutzel, "Multi-modal sensor fusion with machine learning for data-driven process monitoring for additive manufacturing," *Additive Manuf.*, vol. 48, Dec. 2021, Art. no. 102364.

[59] M. Gronle, M. Grasso, E. Granito, F. Schaal, and B. M. Colosimo, "Open data for open science in Industry 4.0: In-situ monitoring of quality in additive manufacturing," *J. Quality Technol.*, vol. 55, no. 2, pp. 253–265, Mar. 2023.

[60] L. Chen, X. Yao, P. Xu, S. K. Moon, and G. Bi, "Rapid surface defect identification for additive manufacturing with in-situ point cloud processing and machine learning," *Virtual Phys. Prototyping*, vol. 16, no. 1, pp. 50–67, Jan. 2021.

[61] I. Garmendia, J. Leunda, J. Pujana, and A. Lamikiz, "In-process height control during laser metal deposition based on structured light 3D scanning," *Proc. CIRP*, vol. 68, pp. 375–380, Jan. 2018.

[62] R. Bernhard, P. Neef, H. Wiche, C. Hoff, J. Hermsdorf, S. Kaierle, and V. Wesling, "Defect detection in additive manufacturing via a toolpath overlaid melt-pool-temperature tomography," *J. Laser Appl.*, vol. 32, no. 2, May 2020, Art. no. 022055.

[63] J.-H. Suh, "Method and system for real-time monitoring and controlling height of deposit by using image photographing and image processing technology in laser cladding and laser-aided direct metal manufacturing process," U.S. Patent 7 423 236, Sep. 9, 2008.

[64] M. Asselin, E. Toyserkani, M. Iravani-Tabrizipour, and A. Khajepour, "Development of trinocular CCD-based optical detector for real-time monitoring of laser cladding," in *Proc. IEEE Int. Conf. Mechatronics Autom.*, Jul. 2005, pp. 1190–1196.

[65] M. Iravani-Tabrizipour and E. Toyserkani, "An image-based feature tracking algorithm for real-time measurement of clad height," *Mach. Vis. Appl.*, vol. 18, no. 6, pp. 343–354, Nov. 2007.

[66] M.-N. Bold, S. Linnenbrink, N. Pirch, A. Gasser, J. Mund, and J. H. Schleifenbaum, "Powder based laser material deposition on edges," *J. Laser Appl.*, vol. 32, no. 3, Aug. 2020, Art. no. 032001.

[67] B. He, D. Li, A. Zhang, J. Ge, X. Yang, and X. Hu, "Influence of scanning pattern on the edge collapse of solid parts in laser metal direct forming," *Opt. Laser Technol.*, vol. 48, pp. 171–177, Jun. 2013.

[68] X. Wang, D. Deng, Y. Hu, F. Ning, H. Wang, W. Cong, and H. Zhang, "Overhang structure and accuracy in laser engineered net shaping of Fe-Cr steel," *Opt. Laser Technol.*, vol. 106, pp. 357–365, Oct. 2018.

[69] A. Nassar and E. Reutzel, "Beyond laser-by-laser additive manufacturing-voxel-wise directed energy deposition," in *Proc. Int. Solid Freeform Fabr. Symp.*, Austin, TX, USA: Univ. Texas at Austin, 2015, pp. 1–11.

[70] A. P. Belchou, A. Jacob, S. Joshi, E. Reutzel, and P. Coutts, "Studies on thin and thick-walled SS316L overhanging specimens manufactured using powder-fed laser-based directed energy," in *Proc. Int. Solid Freeform Fabr. Symp.*, 2022, pp. 1–15.

[71] M. Wang, H. Zhang, Q. Hu, D. Liu, and H. Lammer, "Research and implementation of a non-supporting 3D printing method based on 5-axis dynamic slice algorithm," *Robot. Comput.-Integr. Manuf.*, vol. 57, pp. 496–505, Jun. 2019.

[72] M. Shange, I. Yadroitsava, A. D. Plessis, and I. Yadroitsev, "Roughness and near-surface porosity of unsupported overhangs produced by high-speed laser powder bed fusion," *3D Printing Additive Manuf.*, vol. 9, no. 4, pp. 288–300, Aug. 2022.

[73] D. Knüttel, S. Baraldo, A. Valente, K. Wegener, and E. Carpanzano, "Transfer learning of neural network based process models in direct metal deposition," *Proc. CIRP*, vol. 107, pp. 863–868, Jan. 2022.

[74] R. Liu, S. Liu, and X. Zhang, "A physics-informed machine learning model for porosity analysis in laser powder bed fusion additive manufacturing," *Int. J. Adv. Manuf. Technol.*, vol. 113, nos. 7–8, pp. 1943–1958, Apr. 2021.

[75] H. Al-Khazraji, A. R. Nasser, A. M. Hasan, A. K. Al Mhdawi, H. Al-Raweshidy, and A. J. Humaidi, "Aircraft engines remaining useful life prediction based on a hybrid model of autoencoder and deep belief network," *IEEE Access*, vol. 10, pp. 82156–82163, 2022.

[76] R. H. Hadi, H. N. Hady, A. M. Hasan, A. Al-Jodah, and A. J. Humaidi, "Improved fault classification for predictive maintenance in industrial IoT based on AutoML: A case study of ball-bearing faults," *Processes*, vol. 11, no. 5, p. 1507, May 2023.

[77] F. Kaji, H. Nguyen-Huu, A. Budhwani, J. A. Narayanan, M. Zimny, and E. Toyserkani, "A deep-learning-based in-situ surface anomaly detection methodology for laser directed energy deposition via powder feeding," *J. Manuf. Processes*, vol. 81, pp. 624–637, Sep. 2022.

MUHAMMAD MU'AZ IMRAN received the bachelor's degree from the Faculty of Integrated Technologies, Universiti Brunei Darussalam (UBD), with a major in manufacturing systems engineering. He is currently pursuing the joint Ph.D. degree with the Faculty of Integrated Technologies and the Department of Industrial Engineering, UBD, and Sungkyunkwan University. His research interests include spatiotemporal analysis, machine learning application, metal additive manufacturing, and population synthesis.

YOUNG KIM received the B.Eng. degree in system management engineering from Sungkyunkwan University, where he is currently pursuing the Ph.D. degree with the Department of Industrial Engineering. His current research interests include simulation-based modeling, forecasting method, statistical analysis, and population synthesis.

GISUN JUNG received the B.Eng. degree in system management engineering and the Ph.D. degree in industrial engineering from Sungkyunkwan University. He is currently a Postdoctoral Researcher with the Department of Industrial Engineering, Sungkyunkwan University. His current research interests include demand forecasting, modeling and simulation methodology, data analytics based on stochastic processes, and machine learning.

PG EMEROYLARIFFION ABAS received the B.Eng. degree in information systems engineering and the Ph.D. degree in communication systems from Imperial College, London, in 2001 and 2005, respectively. He is currently a Senior Assistant Professor in system engineering with the Faculty of Integrated Technologies, Universiti Brunei Darussalam. His current research interests include data analysis, the security of info-communication systems, and the design of photonic crystal fiber in fiber optics communication.

LIYANAGE CHANDRATILAK DE SILVA (Senior Member, IEEE) received the B.Sc.Eng. degree (Hons.) from the University of Moratuwa, Sri Lanka, in 1985, the M.Phil. degree from the Open University of Sri Lanka, in 1989, and the M.Eng. and Ph.D. degrees from The University of Tokyo, Japan, in 1992 and 1995, respectively. Currently, he is a Professor and the Dean of the School of Digital Science, Universiti Brunei Darussalam. His current research interests include signal processing (speech and image), the Internet of Things, sensor integration, and power system analysis.

JEONG-HUN SUH received the M.Sc. and Ph.D. degrees from the Korea Advanced Institute of Science and Technology, in 1992. He is currently the Executive Director of Hwacheon Machinery. His research interest includes the development of metal AM, particularly in directed energy deposition.

YUN BAE KIM received the M.S. degree from the University of Florida and the Ph.D. degree from the Rensselaer Polytechnic Institute, New York. He is currently a Professor with the Department of Industrial Engineering, Sungkyunkwan University. His current research interests included metal additive manufacturing focusing on directed energy deposition process, demand forecasting, simulation methodology, epidemiology simulation modeling, high-tech market analysis, and scheduling.

● ● ●